

## Full paper

*Operando* probing ion and electron transport in porous electrodesSingyuk Hou<sup>a</sup>, Tao Gao<sup>a</sup>, Xiaogang Li<sup>a</sup>, Chunsheng Wang<sup>a,b,\*</sup><sup>a</sup> Department of Chemical and Biomolecular Engineering, University of Maryland, College Park, MD, 20740, USA<sup>b</sup> Department of Chemistry and Biochemistry, University of Maryland, College Park, MD, 20740, USA

## ARTICLE INFO

## Keywords:

Porous electrode

Ion and electron transport

Li-ion battery

Energy storage

## ABSTRACT

Utilization of thick and densified electrodes can efficiently increase battery energy density, which is critical for electrical transportation. However, the penalty from ion and electron transport significantly reduces the usable capacity of the electrode and limits the cell level energy density. Mechanistic understanding thus is required to improve electrode design. At present, no experimental method is capable of fully characterizing the kinetic processes, especially ion and electron transport, in porous electrode during dynamic charge and discharge. Here we for the first time measure the potential drops for ion and electron transport in a thick porous electrode during charge/discharge with pulse current cessation in a modified three-electrode cell. Our measurement suggests that capacity loss of a thick electrode at a high rate is highly related to both ion and electron transport potential drops. The potential drops caused by ion and electron transport disintegrates the chemical potential of the active materials in the electrode, thus stop or delay lithiation process of the active materials in the porous electrode. Electrode capacity with phase transformation materials showed higher sensitivities to ion and electron transport potential drops compared to solid solution materials due to different chemical potential profiles upon lithiation.

## 1. Introduction

Porous electrodes in Li-ion batteries consist of active material, carbon conductor and percolated electrolyte. During (de)charge, lithium ions are transported in the percolated electrolyte and electrons are transported through the carbon conductor. Once the ions and electrons neutralize on the surface of active materials, the lithium ions or ambipolars continue moving inside the solid active materials. These transport processes in the porous electrodes cause overpotential and reduce usable capacity, especially on high loading and densified electrodes. As a result, areal loading and thickness of electrode is limited in commercialized Li-ion batteries, leading to more than 50 % loss of energy density from material to cell level [1]. While increasing active material loading is preferred, it is still challenging to achieve due to the elusive limiting process. For example, the transport inside solid active materials is considered to limit electrode capacity due to much lower solid phase diffusivity [2]. However, recent studies showed that electrode capacity is limited by ion transport in the percolated electrolyte as electrode with low tortuosity significantly enhances usable capacity at high rates [3–5]. Similarly, the electron conduction was considered negligible due to the high conductivity of carbon conductor, yet, study using focused ion beam-scanning electron microscopy revealed that insufficient

connectivity between carbon conductor and active material leads to capacity loss [6]. Clarifying these discrepancies is critical for electrode design to meet the requirement of next generation high-energy battery.

Characterization of transport processes in porous electrodes is challenging as they occur simultaneously in both liquid and solid phases [7, 8]. Spectroscopic methods such as Raman confocal spectroscopy, Nuclear Magnetic Resonance, Magnetic Resonance Imaging, X-ray microscope, and Neutron Depth profiling have been successfully used to visualize the ion transport in either bulk electrolyte [9–13] or in the active materials [14–17]. These methods are sensitive to the chemical environment of the probes ( $\text{Li}^+$ , anion or solvent) [18], therefore, it is difficult to develop a single set-up to monitor the behavior in both solid and liquid phase in the porous electrodes. Moreover, the complex composition in porous electrodes can cause interference. For example, Raman signals are influenced by the adsorption or scattering of carbon conductors and active materials [19], and the chemical shift in NMR and MRI distorts near the electrical conductive parts in the electrode [20]. Alternatively, electrochemical methods such as impedance spectroscopy (EIS) and galvanostatic intermittent titration techniques (GITT) characterize multiple transport processes by electrical perturbations. However, diffusions in liquid and solid phase are not distinguishable. Also these methods are operated at low-frequency [21] or near equilibrium,

\* Corresponding author. Department of Chemical and Biomolecular Engineering, University of Maryland, College Park, MD, 20740, USA.

E-mail address: [cswang@umd.edu](mailto:cswang@umd.edu) (C. Wang).<https://doi.org/10.1016/j.nanoen.2019.104254>

Received 1 August 2019; Received in revised form 27 October 2019; Accepted 31 October 2019

Available online 2 November 2019

2211-2855/© 2019 Elsevier Ltd. All rights reserved.

which limits their capability for *operando* measurements. To the best of our knowledge, no experimental method reported so far is capable of characterizing and comparing each transport process in porous electrode.

Considering the transport processes in the electrode are energy dissipations in nature, the corresponding potential drops should provide an appropriate scale for comparison. Here, we measured the potential drops of the transport processes in the porous electrode by accommodating a probing electrode to the three-electrode cell. Deconvolution of the processes was done by choosing the perturbation time (or frequency) that only selected process reacts to (see Table S1 for summary of responding time of the processes in porous electrode). In this study, high loading (20 mg/cm<sup>2</sup>) LiFePO<sub>4</sub> (LFP) and LiNi<sub>0.6</sub>Mn<sub>0.2</sub>Co<sub>0.2</sub>O<sub>2</sub> (NMC 622) porous electrodes were chosen to represent phase transformation and solid solution type active materials. We found that ion and electron transport potential drops in the electrode are mostly responsible for the capacity loss in the porous electrodes. Yet, different active materials showed different sensitivity to ion and electron transport potential drops due to the distinct chemical potential profiles at different lithiation states.

## 2. Results

In the porous electrode, ion diffusion is driven by  $\eta_{diff,i}$ , ion migration is driven by  $\eta_{ohm,i}$  and electron migration is driven by  $\eta_{ohm,e}$ . Since migration of ion and electron responses to external electrical field [22],  $\eta_{ohm}$  is used to represent the summation of the two. The charge transfer on the active material particles is driven by  $\eta_{ct}$  and the lithium transport inside the solid active material is driven by  $\eta_{sol}$ . The summation of these potential drops is the electrode over-potential ( $\eta$ ) (equation (1)).

$$\eta = \eta_{ohm} + \eta_{diff,i} + \eta_{ct} + \eta_{sol} \quad (1)$$

To measure these potential drops, an electrochemical cell (E-cell) in Fig. 1 was designed by accommodating a stainless steel mesh probing electrode (P<sub>1</sub>) into a three-electrode cell with porous working electrode (WE), Li counter (Li CE) and Li reference electrode (Li RE).  $\eta$  is the difference between the equilibrium potential and the operating potential (Fig. 1a) measured in the E-cell. The measurement of other potential

drops involves two subsequent cycles in the E-cell:  $\eta_{ohm} + \eta_{diff,i}$  was obtained by measuring potential between WE and P<sub>1</sub> during charge and discharge (referred to as  $E_1$  in Fig. 1b).  $\eta_{ct}$  was determined by *operando* EIS between WE, CE and RE in the subsequent cycle.  $\eta_{sol}$  can be calculated when other potential drops were determined. The LFP porous WE was used to demonstrate the measurement. In the E-cell, the charge and discharge curves of LFP WE were comparable with that in the standard coin cell tested at 0.2 C (1 C is the current to discharge entire electrode capacity in 1 hour) showing the characteristic flat plateau for phase transformation in LFP (Fig. S1) [23].

### 2.1. Monitoring ion and electron transport potential drops in porous electrode

During galvanostatic charge and discharge, both electrons and ions travel across the porous electrode, generating  $\eta_{ohm} + \eta_{diff,i}$ . These potential drops (refer to as  $E_1$ ) can be measured between P<sub>1</sub> and the current collector (Fig. 2A). Before discharge,  $E_1$  rested at the baseline potential at around 0 mV suggesting the electrode was at equilibrium.  $E_1$  increased abruptly to the transient potential when discharge began and it dropped when discharge ended (Fig. 2A). Noticably, the abrupt drop of  $E_1$  at the end of discharge was followed by a regression to the baseline potential (inset of Fig. 2A). It is known that electron and ion migration respond almost immediately to the variation of external electrical field [24]. Diffusion, on the other hand, responds much slower (see Table S1), therefore the relaxation at the end of discharge should be due to ion diffusion in the percolated electrolyte.

To verify this assumption, we monitored the  $E_1$  after stopping the current at different states of discharge (SODs) (4.5 %, 13 %, 26.7 %, 53.4 %, 80.1 % and at the end of discharge), and calculated the diffusivity (D) from the relaxation profiles (Fig. S2). Combining linear diffusion and Nernst equation (see method for details), a linear relation between  $\ln\left(\exp\left(\frac{E_1}{RT}F\right) - 1\right)$  and  $t$  was found when  $t$  is much larger than the relaxation time for the diffusion process, in which D is implied in the slope (equation (2), R is ideal gas constant,  $T = 298.15$  K is temperature, F is Faraday constant,  $L = 80$   $\mu$ m is the thickness of the electrode). An average  $D = 4.38 \pm 0.6 \times 10^{-7}$  cm<sup>2</sup>/s was obtained using the slopes in

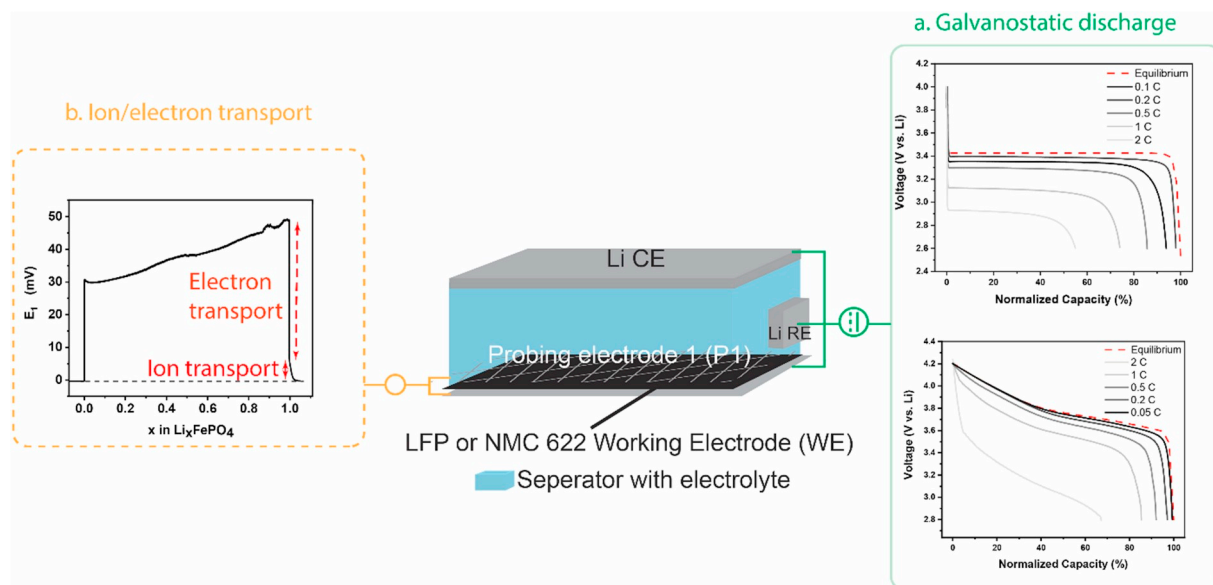


**Fig. 1. The design of E-cell and operando measurement of potential drops.** The E-cell accommodates probing electrode (P<sub>1</sub>) to the three-electrode cell with porous LFP or NMC 622 working electrode (WE), lithium counter electrode (Li CE) and lithium reference electrode (Li RE). **a.** The galvanostatic discharge of LFP (up) and NMC 622 (down) in E-cell. The discharge curves at a variety of C-rates are in solid lines and the equilibrium potentials obtained using galvanostatic intermittent titration technique are in red dash lines. **b.** The potential drops for ionic and electronic transport monitored between current collector and P<sub>1</sub> during charge and discharge.

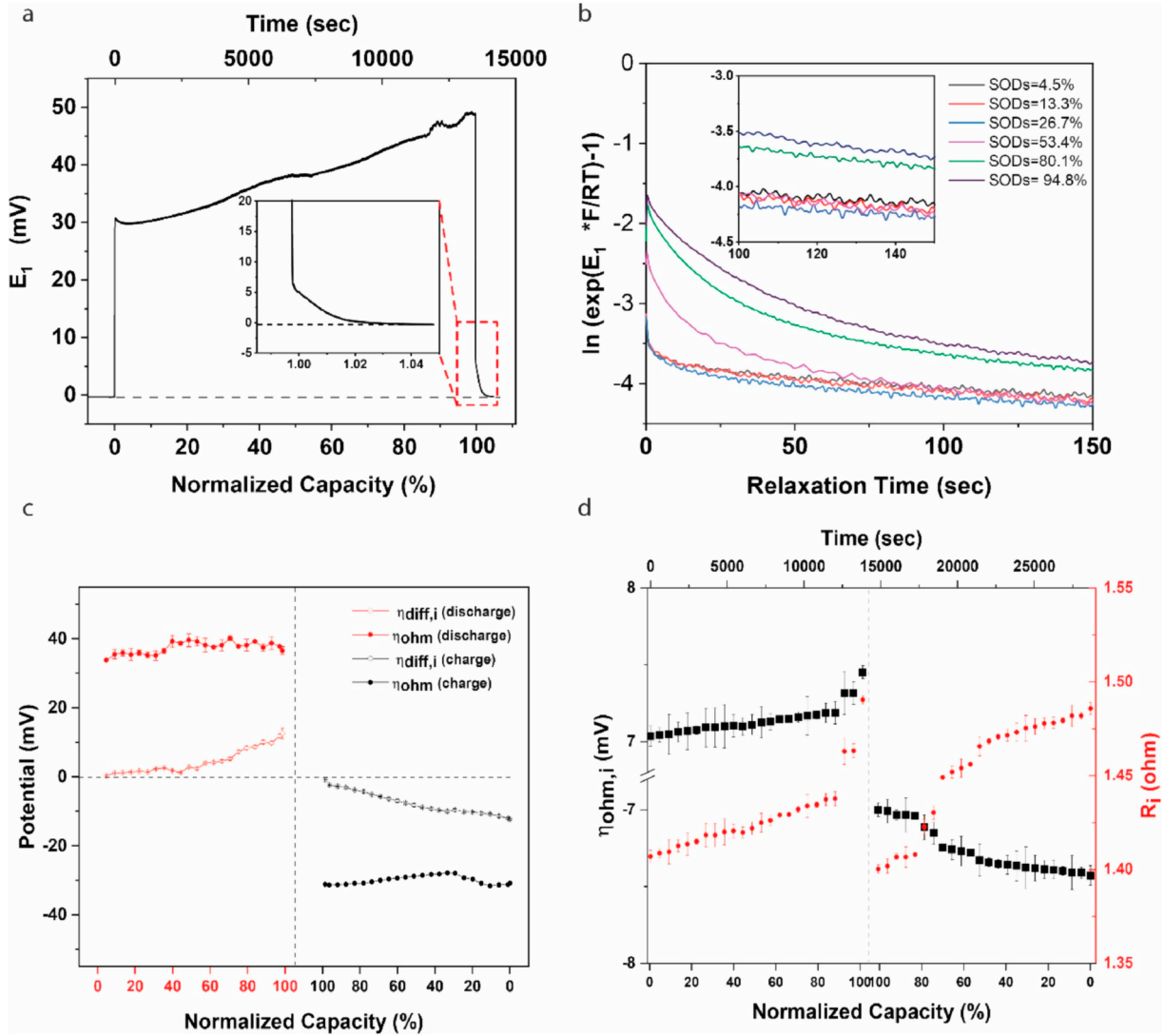


**Fig. 2.** Ion and electron transport in the porous electrode during charge and discharge at 0.2 C. **a.**  $E_1$  profile during discharge. Relaxation of the  $E_1$  at the end of discharge is marked in the red dashed box and the inset. **b.**  $\ln(\exp(\frac{E_1 F}{RT}) - 1)$  -  $t$  plot for the 150-s current cessations at different SODs. Inset shows the linear region after 100 s of relaxation. **c.** The  $\eta_{ohm}$  (dots) and  $\eta_{diff,i}$  (empty dots) determined with 0.5-s pulsed current cessation for every 10 min. The baseline potential of  $E_1$  is marked with black dash line. **d.** The  $R_j$  and  $\eta_{ohm,i}$  during charge and discharge.

the  $\ln(\exp(\frac{E_1 F}{RT}) - 1)$  -  $t$  plots for  $t > 100$  s (inset of Fig. 2B), since all the relaxations stopped at  $t = 100$  s (Fig. S2). It is worth noting that  $D$  obtained here is significantly larger than the lithium diffusivity in LFP particles [2] but smaller than that in bulk electrolyte [25] due to the restricted diffusion in porous electrode. The restricted diffusion was also evidenced by comparing  $D$  to the effective diffusivity ( $D_{eff}$ ) of the electrolyte in porous medium evaluated with Bruggeman correlation [26] ( $D_{eff} = D_{bulk} \times \epsilon^{1.5} = 6.21 \times 10^{-7}$  cm<sup>2</sup>/s, where  $D_{bulk} = 3 \times 10^{-6}$  cm<sup>2</sup>/s represents the diffusivity of  $Li^+$  in the bulk electrolyte [25],  $\epsilon = 0.35$  represents porosity of the electrode). The agreement between  $D_{eff}$  and  $D$  ambiguously demonstrates that the relaxation of  $E_1$  is caused by the diffusion of  $Li^+$  in the percolated electrolyte instead of in the active materials. When  $E_1$  relaxed to the baseline, the  $Li^+$  concentration gradient in the percolated electrolyte was completely eliminated.

$$\ln\left(\exp\left(\frac{E_1 F}{RT}\right) - 1\right) = C - \frac{D}{\pi^2 L^2} * t \left(t \gg \frac{L^2}{D}, C = \text{constant}\right) \quad (2)$$

Due to the different responding times of  $\eta_{diff,i}$  and  $\eta_{ohm}$  to the current cessations,  $\eta_{diff,i}$  at different SODs were determined using 0.5-s pulsed

current cessations during charge and discharge. The 0.5 s was chosen because it is fast enough to not distribute the ion diffusion which has a responding time of tens of seconds (Fig. S2). As the current stopped, spikes were generated in the  $E_1$  profile (Fig. 2C), corresponding to  $\eta_{ohm}$ . The differences between the tips of the spikes and the baseline potential correspond to  $\eta_{diff,i}$  (red empty spots in Fig. 2C). A similar profile for  $\eta_{diff,i}$  was observed during charge but with negative sign (black empty spots in Fig. 2C), as the current and concentration gradient reversed when  $Li^+$  were extracted from the active materials. The steeper  $\eta_{diff,i}$  profile during discharge ( $Li^+$  concentration decreases) and flatter  $\eta_{diff,i}$  profile during charge ( $Li^+$  concentration increases) is due to the asymmetric logarithmic relation between  $\eta_{diff,i}$  and  $Li^+$  concentration. It is worth noting that,  $\eta_{ohm}$  is the summation of ion and electron migration. The contribution from ion migration was determined between WE and an electrically insulated electrode ( $P_2$ ) in a separate cell with *operando* EIS at high frequency ( $10^5$  to  $10^4$  Hz) (Fig. S4). The values of  $\eta_{ohm,i}$  were less than 20 % of  $\eta_{ohm}$ , suggesting that  $\eta_{ohm}$  was mainly caused by electron transport (Fig. 2d). The reproducibility of the measurement was tested after cycling the LFP electrode in this cell following the initial measurement. The capacity of LFP electrode remained stable (Fig. S5),

and similar trends for  $\eta_{\text{diff},i}$  and  $\eta_{\text{ohm}}$  were retrieved after 50 cycles (Figs. S6 and S7).

## 2.2. Measurement of charge transfer potential drops

To obtain charge transfer potential drops  $\eta_{\text{ct}}$ , the charge transfer resistance ( $R_{\text{ct}}$ ) of LFP electrode was measured between WE, Li RE and Li CE during discharge by *operando* EIS. To make sure that the semi-circles observed in *operando* EIS is actually due to the charge transfer instead of other capacitive processes, the characteristic frequency for the semi-circle during discharge was compared with that at equilibrium. Good agreement of the characteristic frequencies was found between equilibrium and *operando* EIS for the charge transfer semi-circle observed between 400–500 Hz (Fig. S8). The Nyquist plots for the *operando* EIS showed suppressed semicircles at the same frequency range, suggesting that the same charge transfer process was measured (Fig. S9). Thus the  $R_{\text{ct}}$  was obtained at the frequency between  $10^5$  to 50 Hz for charge transfer without affecting diffusion. The  $\eta_{\text{ct}}$  was related to  $R_{\text{ct}}$  through Butler-Volmer kinetics.

## 2.3. The role of ion and electron transport on electrode capacity

Lithium storage in LFP proceeds with phase transformation within the miscibility gap. This process was represented by the steady regions in the  $\eta_{\text{sol}}$  profiles (Fig. 3a), in which the movement of Li in LFP is maintained by the constant  $\eta_{\text{sol}}$  attributed to constant lithium diffusivity [23]. The steady regions of  $\eta_{\text{sol}}$  shortened from 90% SODs at 0.1 C to 50% SODs at 2 C (Fig. 3a), but phase transformation was able to proceed with  $\eta_{\text{sol}}$  (around 50 mV) smaller than potential drops of any other processes at 2 C (Fig. 3b–d). Therefore, the capacity loss in LFP electrode should not be caused by phase transformation kinetics within particles, but rather the reduced number of particles that finished phase transformation. To determine the processes that stop the phase

transformation, regression analysis was performed using  $\eta_{\text{diff},i}$ ,  $\eta_{\text{ohm}}$ , and  $\eta_{\text{ct}}$  at the end of discharge as predictors. The larger standard coefficient for  $\eta_{\text{diff},i}$  and  $\eta_{\text{ohm}}$  suggests that ionic transport in electrolyte and electron transport have greater effect on capacity loss (Fig. 3e). This finding aligns with the traditional believe that drastic capacity drop observed in the capacity retention versus C-rate plot (Fig. S10) is caused by transport limitation in the electrolyte [27,28]. In addition,  $\eta_{\text{diff},i}$  profiles further suggested that the drastic capacity drops could occur simply with  $\text{Li}^+$  concentration gradient before ion depletion in the electrolyte, since the exponential increase of  $\eta_{\text{diff},i}$  to infinity caused by zero  $\text{Li}^+$  concentration was not observed in these rates (Fig. 3b). In addition, even though no significant loss of electrical contact inside the electrode during lithiation, as evidenced by the constant or slightly decreasing  $\eta_{\text{ohm}}$  (Fig. 3c), the effect of electron transport was also pronounced. These evidences suggested that  $\eta_{\text{diff},i}$  and  $\eta_{\text{ohm}}$  across the electrode at higher rates reduced electrode capacity by stopping phase transformation in some of the LFP particles without complete ion depletion or electrical contact loss.

Based on the results from LFP electrode, we hypothesized that active materials that do not undergo phase transformation should be less affected by  $\eta_{\text{diff},i}$  and  $\eta_{\text{ohm}}$ . NMC 622, a material known to form solid solution upon lithiation, was then used for the same measurement [29–31]. To avoid electrolyte decomposition and structural change in NMC 622, the operation range was from 2.7 to 4.2 V vs. Li and the usable capacity was normalized to the capacity obtained from GITT in this range (Fig. S11). Lithiation in NMC 622 was driven by tilted  $\eta_{\text{sol}}$  due to the decreasing Li diffusivity inside NMC 622 upon lithiation [30]. The tilted region in  $\eta_{\text{sol}}$  profiles reduced from 90 % SODs at 0.05 C to 70 % SODs at 2 C, which is only half of that in LFP electrode (reduced by 40 %), showing better capacity retention (Fig. 4a). It is worth noting that the value of  $\eta_{\text{sol}}$  in NMC 622 are significantly larger than that in LFP at 2C, therefore the better capacity retention was not due to faster solid phase transport (Fig. 4a). The value of  $\eta_{\text{diff},i}$  in NMC 622 was similar to that in LFP electrode since both electrodes have the same porosity

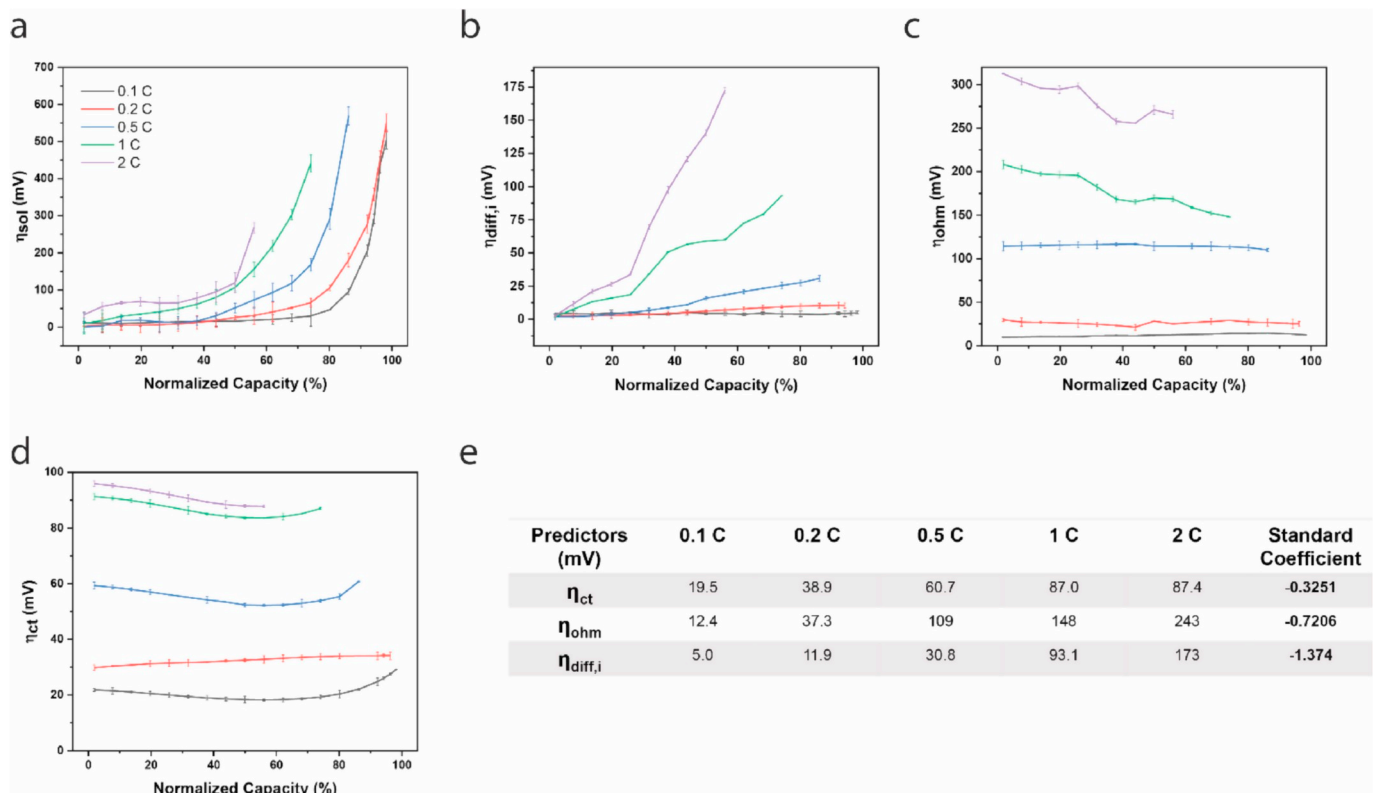
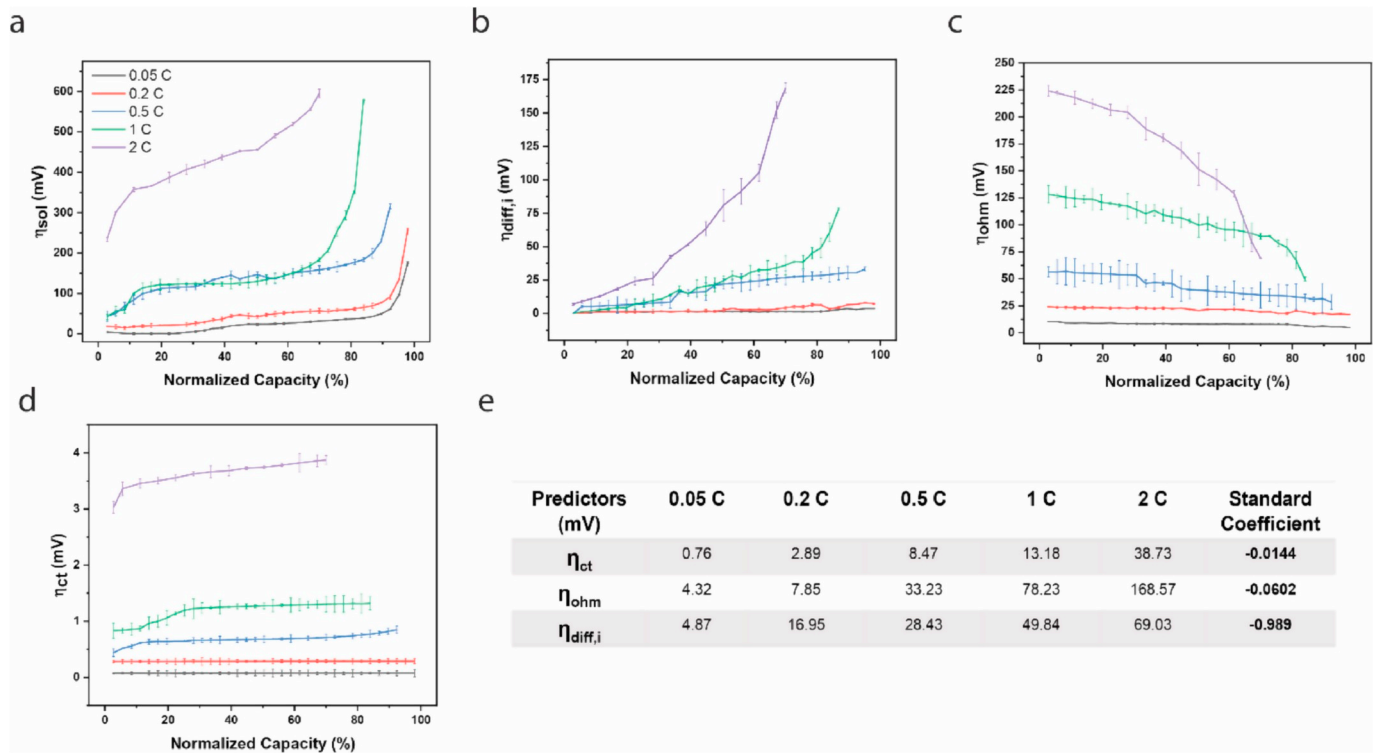


Fig. 3. Potential drops in LFP electrode at different SODs when operated at 0.1 C, 0.2 C, 0.5 C, 1 C and 2 C. a–d.  $\eta_{\text{sol}}$ ,  $\eta_{\text{diff},i}$ ,  $\eta_{\text{ohm}}$ , and  $\eta_{\text{ct}}$ . e. Regression analysis using potential drops at the end of discharge as predictors,  $R^2 = 0.99996$ .





**Fig. 4.** Potential drops of the porous NMC 622 electrode at different SODs when operated at 0.05, 0.2, 0.5, 1 and 2 C. a-d,  $\eta_{sol}$ ,  $\eta_{diff,i}$ ,  $\eta_{ohm}$ , and  $\eta_{ct}$ . f. Multiple regression using the potential drops at the end of discharge as predictors,  $R^2 = 0.99999$ .

(Fig. 4b). However,  $\eta_{ohm}$  for NMC 622 electrode was observably smaller than that of LFP electrode at the same rate, the decrease of  $\eta_{ohm}$  with SODs also suggested that the lithiated NMC 622 participated in forming a more effective conduction network for electron transport (Fig. 4c). To

identify whether the better capacity retention of NMC 622 electrode at high rate is due to the smaller  $\eta_{ohm}$  or that NMC 622 is less sensitive to  $\eta_{ohm}$  and  $\eta_{diff,i}$ , regression analysis was performed. The significantly smaller standard coefficients for  $\eta_{ohm}$  and  $\eta_{diff,i}$  supports our assumption

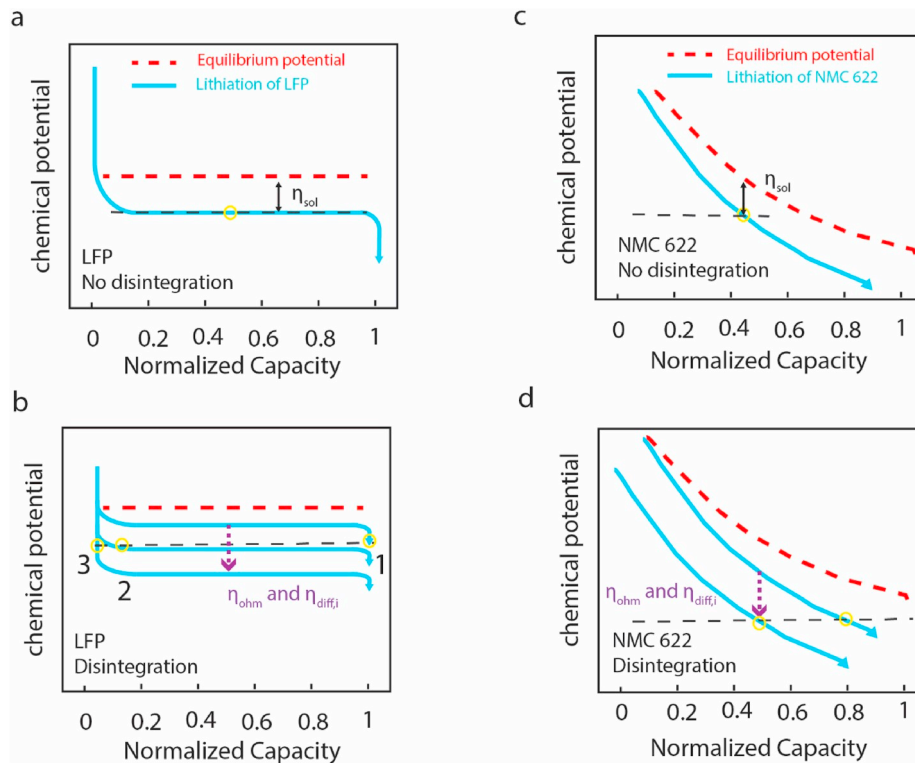


**Fig. 5.** Disintegration of particle chemical potential. a. Chemical potential profile of LFP particle; b. Disintegration of particle chemical potential in LFP electrode; c. Chemical potential profile of NMC 622; d. Disintegration of particle chemical potential in NMC 622 electrode.

that material without phase transformation are less sensitive to  $\eta_{ohm}$  and  $\eta_{diff,i}$  in the electrode (Fig. 4e).

A mechanism was proposed to understand the different capacity retentions of NMC 622 and LFP under the influence of  $\eta_{ohm}$  and  $\eta_{diff,i}$  at high rate. When electrodes were operated at low rate (0.1 C or below),  $\eta_{ohm}$  and  $\eta_{diff,i}$  across the electrode are negligible and the potentials of the particles in the electrode are the same, the  $\eta_{sol}$  reflects the driving force needed to lithiating each particle. For LFP particles, phase transformation proceeds with a steady  $\eta_{sol}$  from lithium-poor to lithium-rich phase (blue in Fig. 5a) and for NMC 622 particles, lithiation proceeds with an enhancing  $\eta_{sol}$  (blue in Fig. 5c). At high rate, the increasing  $\eta_{ohm}$  and  $\eta_{diff,i}$  across the electrode disintegrate the potential of the active material particles in the electrodes. When the potentials of the LFP particles in the porous electrode are disintegrated, the particles with higher potentials are driven to lithium-rich phase by a given  $\eta_{ohm}$  (number 1 in Fig. 5b). This  $\eta_{ohm}$ , however, is not enough to drive the lithiation of low potential particles (number 2 and 3 in Fig. 5b). As a result, the phase transformation proceed in high potential particles with relatively small  $\eta_{sol}$  but not in the low potential particles, reducing the electrode capacity. When the potential of NMC 622 particles are disintegrated, the high potential particles are driven to higher SODs by the  $\eta_{sol}$ , this  $\eta_{sol}$  can drive the lithiation of low potential particles to lower SODs. As the  $\eta_{sol}$  increased, the low potential particles can be further lithiated, therefore only delay the lithiation process in the low potential particles (Fig. 5d), manifested as better capacity retention.

The lithiation behavior of active materials were usually study in thin electrodes, in which  $\eta_{ohm}$  and  $\eta_{diff,i}$  are not significant (Fig. S12). However, our study demonstrated that  $\eta_{ohm}$  and  $\eta_{diff,i}$  can stop or delay the (de)lithiation process in high loading electrode and eventually cause capacity loss. The effect depends on the chemical potential profile of the active materials, thus providing another dimension to alleviate capacity loss due to insufficient ion and electron transport in high loading electrodes. While in some cases  $\eta_{ct}$  is important, the magnitude and the standard coefficients of  $\eta_{ct}$  were relatively small, thus they were not extensively discussed in this study (Figs. 3d and 4d).

From the technical aspect, the lithium metal used in this study could consume the carbonate electrolyte over long-term cycling. But the effect was not significant within 50 cycles as demonstrated by the similar  $E_1$  measured after 50 cycles in Figs. S6 and S7. If the ion or electron transport potential drops in the porous electrode are to be determined over extensive cycling, more stable reference and counter electrodes such as  $Li_4Ti_5O_{12}$  or  $LiFePO_4$  [32,33] could be used instead of the lithium metal.

### 3. Conclusion

In this study, an E-cell was built to measure the potential drops caused by ion and electron transport. For the first time, we demonstrated the dynamic variation of each transport process using high loading porous LFP and NMC 622 electrodes. The regression analysis demonstrated that the loss of electrode capacity is highly related to ion and electron transport, but does not necessarily required ion depletion or loss of electrical contact. The underlying reason is that the ion and electron transport potential drops disintegrate lithium chemical potential of the particles in the electrodes, stopping the lithiation process. Due to different lithiation mechanisms, the capacity loss of LFP and NMC 622 electrodes showed different sensitivity to the ion and electron transport potential drops. The method presented in this study is affordable and independent to active material or electrolyte used. For boarder applications, it can be used to understand how different electrode designs affect the performance, especially for hierarchical or flexible structures that cannot be efficiently predicted with numerical models.

## 4. Experimental methods

### 4.1. Electrode and electrolyte preparation

The electrolyte was prepared by dissolving the  $LiPF_6$  (Sigma Aldrich) in the ethylene carbonate/dimethyl carbonate (50/50 wt %) to form a 1 M solution. NMC 622 (20 mg/cm<sup>2</sup> active material) with 80  $\mu$ m thickness, 35% porosity and LFP electrodes (20 mg/cm<sup>2</sup> active material) with porosity of 35% and thickness of 80  $\mu$ m were obtained from Saft Batteries, the gravimetric ratio between Kejan black coated LFP particle or NMC 622 particle, carbon black and PVDF is 9: 0.5: 0.5. The size distribution of LFP particles peaks at around 300–500 nm (SEM figure of the electrode and histogram in Fig. S12).

### 4.2. Electrochemical cell fabrication

The electrochemical cell (E-cell) consists of a substrate and a lid machined from polytetrafluoroethylene rod. The center of the substrate was caved with a  $3 \times 3 \times 1.5$  cm (length/width/depth) indentation, in which the  $3 \times 3$  cm (length/width) WE, CE and  $2.5 \times 2.5$  cm (length/width)  $P_1$  were assembled in layer-by-layer manner and fit into a folded 25  $\mu$ m Celgard separator ( $6 \times 3.5$  cm). The smaller  $P_1$  was used to avoid contact with the current collectors for WE and CE. A small piece of Li reference electrode was placed on the side of the electrode stacks. The electrode stack was secured by stainless steel spacer and spring. After cell assembly, the substrate and the cover were lodged by screws to avoid exposure to air and humidity.

### 4.3. Electrochemical analysis

All the electrochemical experiments were performed in the E-cell unless stated otherwise. The galvanostatic charge/discharge was performed using Arbin battery test station, with designated C-rate density for discharge and a fixed current density of 0.2 C (corresponding to 0.55 mA/cm<sup>2</sup> for the thick electrode and 0.22 mA/cm<sup>2</sup> for charge. The corresponding cutoff potentials were 2.6 V–4.0 V vs the Li CE for LFP, 2.7 V–4.2 V vs Li CE for NMC 622. To ensure all the LFP particles are fully delithiated, charge was followed by a 2 hour constant voltage charging at 4.0 V. The 4.2 V cut-off potential for NMC 622 is to avoid electrolyte or active material decomposition and maintain similar specific capacity compared to LFP. The 0.5-s current cessations were performed for each 15 min at 0.1 C, 0.2 C and 0.5 C, for each 5 min for 1 C and 2 C.  $E_1$  was measured using Arbin battery test station with time resolution of 0.1 s to ensure variation of  $E_1$  during the current cessation was captured. The *operando* EIS measurement was performed with Gamary interface 1000 using 5 mV perturbation with the desired frequency range for each 15 min at 0.1 C, 0.2 C and 0.5 C, for each 5 min for 1 C and 2 C to match the resolution of current cessation.

### 4.4. Linear diffusion model

The concentration of Li ion in the electrolyte during current cessation can be expressed as followed:

$$\frac{\partial C_{Li^+}}{\partial t} = -D \cdot \frac{\partial^2 C_{Li^+}}{\partial x^2}$$

Boundary conditions for current cessation (the position of current collector ( $E_1$ ) is set to be  $x = 0$ ):

$$C_{Li^+}(x = 0, t = \infty) = C_0$$

$$\frac{\partial C_{Li^+}}{\partial x}(x = 0) = 0$$

$$C_{Li^+}(x = \infty) = C_0$$

The relationship between the Li ion concentration and the potential

sensed at  $E_1$  and  $P_1$  can be expressed with Nernst equation:

$$E = E^0 + \frac{RT}{F} \ln \left( \frac{C_{Li^+}}{a_{Li, LFP}} \right)$$

where  $E^0$  is the equilibrium potential of the LFP electrode;  $a_{Li, LFP}$  is the activity of Li in LFP, which was considered to be constant across the electrode;  $R$  is the ideal gas constant,  $T$  is temperature and  $F$  is the Faraday constant.

## Declaration of competing interest

The authors declare that they have no known competing financial interests or personal relationships that could have appeared to influence the work reported in this paper.

## Acknowledgements

The authors gratefully acknowledge the Nanostructures for Electrical Energy Storage, an Energy Frontier Research Center (award number DESC0001160) and the Battery 500 Consortium (award number DE-EE0008200) for their support.

## Appendix A. Supplementary data

Supplementary data to this article can be found online at <https://doi.org/10.1016/j.nanoen.2019.104254>.

## References

- [1] D. Andre, et al., Future generations of cathode materials: an automotive industry perspective, *J. Mater. Chem.* 3 (2015) 6709–6732.
- [2] M. Park, X. Zhang, M. Chung, G.B. Less, A.M. Sastry, A review of conduction phenomena in Li-ion batteries, *J. Power Sources* 195 (2010) 7904–7929.
- [3] C.J. Bae, C.K. Erdonmez, J.W. Halloran, Y.M. Chiang, Design of battery electrodes with dual-scale porosity to minimize tortuosity and maximize performance, *Adv. Mater.* 25 (2013) 1254–1258.
- [4] J.S. Sander, R.M. Erb, L. Li, A. Gurijala, Y.M. Chiang, High-performance battery electrodes via magnetic templating, *Nat. Energy* 1 (2016).
- [5] J. Billaud, F. Bouville, T. Magrini, C. Villevieille, A.R. Studart, Magnetically aligned graphite electrodes for high-rate performance Li-ion batteries, *Nat. Energy* 1 (2016).
- [6] N. Besnard, et al., Multiscale morphological and electrical characterization of charge transport limitations to the power performance of positive electrode blends for lithium-ion batteries, *Adv. Energy Mater.* 7 (2017) 1602239.
- [7] K.S.W. Sing, Characterization of porous materials: past, present and future, *Colloid. Surf. Physicochem. Eng. Asp.* 241 (2004) 3–7.
- [8] D.R. Rolison, et al., Multifunctional 3D nanoarchitectures for energy storage and conversion, *Chem. Soc. Rev.* 38 (2009) 226–252.
- [9] M. Klett, et al., Quantifying mass transport during polarization in a Li Ion battery electrolyte by in situ  $^7\text{Li}$  NMR imaging, *J. Am. Chem. Soc.* 134 (2012) 14654–14657.
- [10] S.A. Krachkovskiy, et al., Visualization of steady-state ionic concentration profiles formed in electrolytes during Li-ion battery operation and determination of mass-transport properties by in situ magnetic resonance imaging, *J. Am. Chem. Soc.* 138 (2016) 7992–7999.
- [11] M.M. Britton, P.M. Bayley, P.C. Howlett, A.J. Davenport, M. Forsyth, In situ, real-time visualization of electrochemistry using magnetic resonance imaging, *J. Phys. Chem. Lett.* 4 (2013) 3019–3023.
- [12] J.D. Forster, S.J. Harris, J.J. Urban, Mapping  $\text{Li}^+$  concentration and transport via in situ confocal Raman microscopy, *J. Phys. Chem. Lett.* 5 (2014) 2007–2011.
- [13] D. Takamatsu, A. Yoneyama, Y. Asari, T. Hirano, Quantitative visualization of salt concentration distributions in lithium-ion battery electrolytes during battery operation using X-ray Phase Imaging, *J. Am. Chem. Soc.* 140 (2018) 1608–1611.
- [14] W.C. Chueh, et al., Intercalation pathway in many-particle  $\text{LiFePO}_4$  electrode revealed by nanoscale state-of-charge mapping, *Nano Lett.* 13 (2013) 866–872.
- [15] X. Zhang, T.W. Verhallen, F. Labohm, M. Wagemaker, Direct observation of Li-ion transport in electrodes under nonequilibrium conditions using neutron depth profiling, *Adv. Energy Mater.* 5 (2015) 1–8.
- [16] J.F.M. Oudenhoven, et al., In situ neutron depth profiling: a powerful method to probe lithium transport in micro-batteries, *Adv. Mater.* 23 (2011) 4103–4106.
- [17] S.I. Nishimura, et al., Experimental visualization of lithium diffusion in  $\text{LiFePO}_4$ , *Nat. Mater.* 7 (2008) 707–711.
- [18] P.P.R.M.L. Harks, F.M. Mulder, P.H.L. Notten, In situ methods for Li-ion battery research: a review of recent developments, *J. Power Sources* 288 (2015) 92–105.
- [19] K. Ray, R.L. McCreery, Spatially resolved Raman spectroscopy of carbon electrode surfaces: observations of structural and chemical heterogeneity, *Anal. Chem.* 69 (1997) 4680–4687.
- [20] A.D. Buckingham, E.G. Lovering, Effects of a strong electric field on NMR spectra: the absolute sign of the spin coupling constant, *Trans. Faraday Soc.* 67 (1962) 2077–2081.
- [21] E. Barsoukov, J.R. Macdonald, Impedance Spectroscopy. Impedance Spectroscopy: Theory, Experiment, and Applications, Wiley, New Jersey, 2005.
- [22] A.J. Bard, R.F. Larry, L. Johna, G.Z. Cynthia, *Electrochemical Methods: Fundamentals and Applications*, vol. 2, Wiley, New York, 1980.
- [23] Y. Zhu, C. Wang, Galvanostatic intermittent titration technique for phase-transformation electrodes, *J. Phys. Chem. C* 114 (2010) 2830–2841.
- [24] A.J. Bard, R.F. Larry, L. Johna, G.Z. Cynthia, *Electrochemical Methods: Fundamentals and Applications*, vol. 2, Wiley, New York, 1980.
- [25] L.O. Valøen, J.N. Reimers, Transport properties of  $\text{LiPF}_6$ -based Li-ion battery electrolytes, *J. Electrochem. Soc.* 152 (2005) A882–A891.
- [26] B. Tjaden, S.J. Cooper, D.J. Brett, D. Kramer, P.R. Shearing, On the origin and application of the Bruggeman correlation for analysing transport phenomena in electrochemical systems, *Curr. Opin. Chem. Eng.* 12 (2016) 44–51.
- [27] T.R. Ferguson, M.Z. Bazant, Nonequilibrium thermodynamics of porous electrodes, *J. Electrochem. Soc.* 159 (2012) A1967–A1985.
- [28] C. Heubner, J. Nickol, J. Seeba, S. Reuber, N. Junker, M. Wolter, M. Schneider, A. Michaelis, Understanding thickness and porosity effects on the electrochemical performance of  $\text{LiNi}_{0.6}\text{Co}_{0.2}\text{Mn}_{0.2}\text{O}_2$ -based cathodes for high energy Li-ion batteries, *J. Power Sources* 419 (2019) 119–123.
- [29] M.S. Whittingham, Ultimate limits to intercalation reactions for lithium batteries, *Chem. Rev.* 114 (2014) 11414–11443.
- [30] S. Cui, et al., Optimized temperature effect of Li-ion diffusion with layer distance in  $\text{Li}(\text{Ni} \times \text{Mn} \times \text{Co} \times \text{O})_2$  cathode materials for high performance Li-ion battery, *Adv. Energy Mater.* 6 (2016) 1501309.
- [31] A. Van der Ven, J. Bhattacharya, A.A. Belak, Understanding Li diffusion in Li-intercalation compounds, *Acc. Chem. Res.* 46 (2013) 1216–1225.
- [32] J. Wandt, J. Lee, D.W.M. Arrigan, D.S. Silvester, A lithium iron phosphate reference electrode for ionic liquid electrolytes, *Electrochem. Commun.* 93 (2018) 148–151.
- [33] F. La Mantia, C.D. Wessells, H.D. Deshaizer, Y. Cui, Reliable reference electrodes for lithium-ion batteries, *Electrochem. Commun.* 31 (2013) 141–144.